



Nanoscale

Dipole modelling for a robust description of subdiffractive polariton waves

Journal:	<i>Nanoscale</i>
Manuscript ID	NR-ART-08-2019-007387.R1
Article Type:	Paper
Date Submitted by the Author:	04-Oct-2019
Complete List of Authors:	<p>Feres, Flávio; CNPEM, Brazilian Synchrotron Light Laboratory Barcelos, Ingrid; Universidade Federal de Minas Gerais, Departamento de Física Mayer, Rafael; CNPEM, Brazilian Synchrotron Light Laboratory Miguel, Thiago; CNPEM, Brazilian Synchrotron Light Laboratory Freitas, Raul; Centro Nacional de Pesquisa em Energia e Materiais (CNPEM), Laboratório Nacional de Luz Sincrotron (LNLS) Raschke, Markus; University of Colorado, Physics; University of Washington Department of Chemistry, Bahamon, Dario; Mackenzie Presbyterian University, MackGraphe-Graphene and Nano-Materials Research Center Barbosa Maia, Francisco ; Brazilian Center for Research in Energy and Materials (CNPEM), Brazilian Synchrotron Light Laboratory (LNLS)</p>

SCHOLARONE™
Manuscripts

Dipole modelling for a robust description of subdiffractive polariton waves

Flávio H. Feres^{1,2}, Ingrid D. Barcelos¹, Rafael A. Mayer^{1,3}, Thiago M. dos Santos¹, Raul O. Freitas¹, Markus B. Raschke⁴, Dario A. Bahamon⁵ and Francisco C. B. Maia^{1,*}

1 - Brazilian Synchrotron Light Laboratory (LNLS), Brazilian Center for Research in Energy and Materials (CNPEM), Zip Code 13083-970, Campinas, Sao Paulo, Brazil.

2 - Physics Department, Institute of Geosciences and Exact Sciences, São Paulo State University – UNESP, Rio Claro 13506-900, Brazil

3 – Physics Department, Gleb Wataghin Physics Institute, University of Campinas (Unicamp), 13083-859 Campinas, Sao Paulo, Brazil

4 - Department of Physics, Department of Chemistry, and JILA, University of Colorado, Boulder, Colorado 80309, United States.

5 - MackGraphe - Graphene and Nanomaterials Research Center, Mackenzie Presbyterian University, 01302-907, São Paulo, Brazil

*Corresponding Author: francisco.maia@lnls.br

Abstract

The nanophotonics of van der Waals (vdW) materials relies critically on the electromagnetic properties of polaritons defined on sub-diffraction length scales. Here, we use a full electromagnetic Hertzian dipole antenna (HDA) model to describe the hyperbolic phonon polaritons (HP²) in vdW crystals of hexagonal boron nitride (hBN) on a gold surface. The HP² waves are investigated by broadband synchrotron infrared nanospectroscopy (SINS) which covers the type I and type II hyperbolic bands simultaneously. Basically, polariton waves, observed by SINS, are assigned to the resultant electric field from the summation over the irradiated electric field of dipoles distributed along the crystal edge and at the tip location and a non-propagating field. The values of polariton momenta and damping extracted from the HDA model present excellent agreement with theoretical predictions. Our analysis shows that the confinement factor of type I HP₂'s exceeds that of type II ones by up to a factor of 3. We extract anti-parallel group velocities (v_g) for type I ($v_{g,type I} = -0.005c$, c is the light velocity in vacuum) in relation to type II ($v_{g,type II} = 0.05c$) polaritonic pulses, with lifetimes of ~ 0.6 ps and ~ 0.3 ps, respectively. Further, by incorporating consolidated optical-near field theory into the HDA model, we simulate real-space images of polaritonic standing waves for hBN crystals of different shapes. This approach reproduces the experiments with minimal computational cost. Thus, it is demonstrated that the HDA modelling self-consistently explains the measured complex-valued polariton near-field, while being a general approach applicable to other polariton types, like plasmon- and exciton-polaritons, active in the wide range of vdW materials.

Introduction. Phonon-polaritons¹⁻³ are hybrid electromagnetic modes of polarizable media in the form of collective phononic excitations resonantly coupled with the infrared (IR) excitation field. In hexagonal boron nitride (hBN) van der Waals (vdW) crystals as example, subwavelength hyperbolic phonon-polaritons (HP²) lead to intriguingly strong and exotic light-matter interactions¹⁻⁴. In general, these subdiffractive electromagnetic modes are supported by anisotropic crystals with hyperbolic dispersion relations conventionally visualized by plots of excitation frequency ω versus polariton momentum q_p . The hyperbolic behavior of hBN emerges in the spectral region where the real parts of the in-plane ϵ_{\perp} and out-of-plane ϵ_{\parallel} components of the permittivity tensor $\vec{\epsilon}$ [$\vec{\epsilon} = (\epsilon_{\perp}, \epsilon_{\perp}, \epsilon_{\parallel})$ with the \perp and \parallel symbols defined with respect to the \mathbf{c} axis of hBN, see supporting information] have opposite signs, i.e., $Re(\epsilon_{\perp}) \cdot Re(\epsilon_{\parallel}) < 0$. Hyperbolic crystals are therefore also coined indefinite media⁵ since the hyperbolic nature of $\omega - q_p$ permits the HP² wavelength λ_p ($\lambda_p = 2\pi/q_p$) to be much shorter than the corresponding free-space excitation wavelength λ_{IR} . hBN possesses type I and type II hyperbolic bands featuring characteristic polaritons spectrally separated in the mid-IR spectrum. The type I band spans the range of 13.33 - 12.2 μm (750 - 820 cm^{-1}), wherein $Re(\epsilon_{\parallel}) < 0$ and $Re(\epsilon_{\perp}) > 0$. Correspondingly, type I HP²s are formed by the mid-IR field hybridized with out-of-plane polarized phonons. On the other hand, type II HP²s are excited by 7.33 - 6.21 μm (1365 - 1610 cm^{-1}) light coupled to in-plane polarized phonons.

HP²s in hBN-based systems⁶⁻⁸ have been intensely studied by scattering-scanning near field optical microscopy (s-SNOM)⁹⁻¹¹, Synchrotron Infrared Nanospectroscopy (SINS)^{12,13} and by photo-induced near-field force microscopy (AFM-IR/PiFM)¹⁴. Those techniques have provided real-space images of HP² standing waves¹⁵⁻¹⁷, uncovering diverse aspects like the λ_p dependence on crystal thickness⁴ and on substrate permittivity^{16,18-20}, strong light confinement⁸ with $\lambda_{IR}/\lambda_p \sim 50$ ¹, ultra-low group velocity^{6,21}, ability of imaging, focusing and guiding at subwavelength regimes²²⁻²⁴, propagation with atypical convex wavefronts²⁵ and hybridization¹² with graphene plasmon-polaritons^{18,12,26} in graphene-hBN heterostructures. Most of those studies focused on type II HP² waves that are spectrally accessible by commercially available mid-IR quantum cascade lasers (QCL), which are largely used for imaging. In contrast, fewer studies have accessed type I HP²s^{13,22,23,27-29}, whose longer-wavelength range, although also recently accessed by QCL's⁶, generally requires more specialized IR sources as available via optical parametric generation and synchrotrons.

In general, the main launchers of polariton waves are ascribed to the metallic probe tip^{6,8,29}, crystal wrinkles^{20,33}, rounded²³ and linear-like^{21,22,31} nano-antennas and edges of the hBN crystal^{6,20,31,34}. The primarily determined polariton property is q_p , which is typically extracted from experimental profiles by Fourier transform processing²³ or from fit models concerning damped sine²⁹ or adapted models of 2D systems^{20,31,35}. On the other hand, it has been observed HP² modes propagating as plane waves launched by the edges of the crystal^{6,34} and Au pads²¹. Such different approaches indicate that the modelling of the phonon-polariton waves, while being still a subject under discussion, has an intrinsic dependence on the polariton launchers. We address to this problem by proposing a full electromagnetic modelling based on simple dipole

distribution. The model is used to explain the two types of HP² waves measured in hBN lying on Au and on SiO₂ substrates (supplement) using SINS. In this framework, the polariton launchers, which are located in regions close to the crystal submitted to strong optical polarization, are represented by Hertzian dipole antennas (HDA) treated as the emitting sources of the polariton waves. By considering the vector potential of each dipole, the expressions of their irradiated electric fields are derived from Maxwell equations (supplement). Thereby, the observed polariton wave is assigned to the analytic resultant electric field given by the summation over the irradiated electric fields of all dipoles.

In further details, the tip and edge, which are typical polariton launchers^{6,8}, are replaced by a single HDA and a discrete distribution of HDAs, respectively (Figure 1a). The total polariton electric field at any given site is produced by the interference of the irradiated electric fields of the dipoles. The analytic expression of the resultant polariton electric field is then used to fit the HP² standing waves observed from SINS spectral linescans. The model-determined $\omega - q_p$ and values of group velocity (v_g) and life-time (τ) match theoretical predictions⁴ for in- and out-of-plane polarized polaritons and agree with previous reports^{15–17,22–24}. It is demonstrated that the approach is self-consistent since the phase of the polariton wave is generated from the parameters of corresponding amplitude. Therefore, the model fulfills the Kramers-Kronig relation. In combination with the finite dipole model theory, the HDA model simulates real space HP² standing waves in hBN, with arbitrary geometries, in agreement with the experiment and at low computational cost. In the following, we first present SINS spectral linescans over the type I and type II bands. The HDA model is described and used to fit the polariton waves extracted from SINS. Then, fit-determined $\omega - q_p$, v_g and τ are discussed. Finally, we compare simulated and experimental images for type I and type II polaritons.

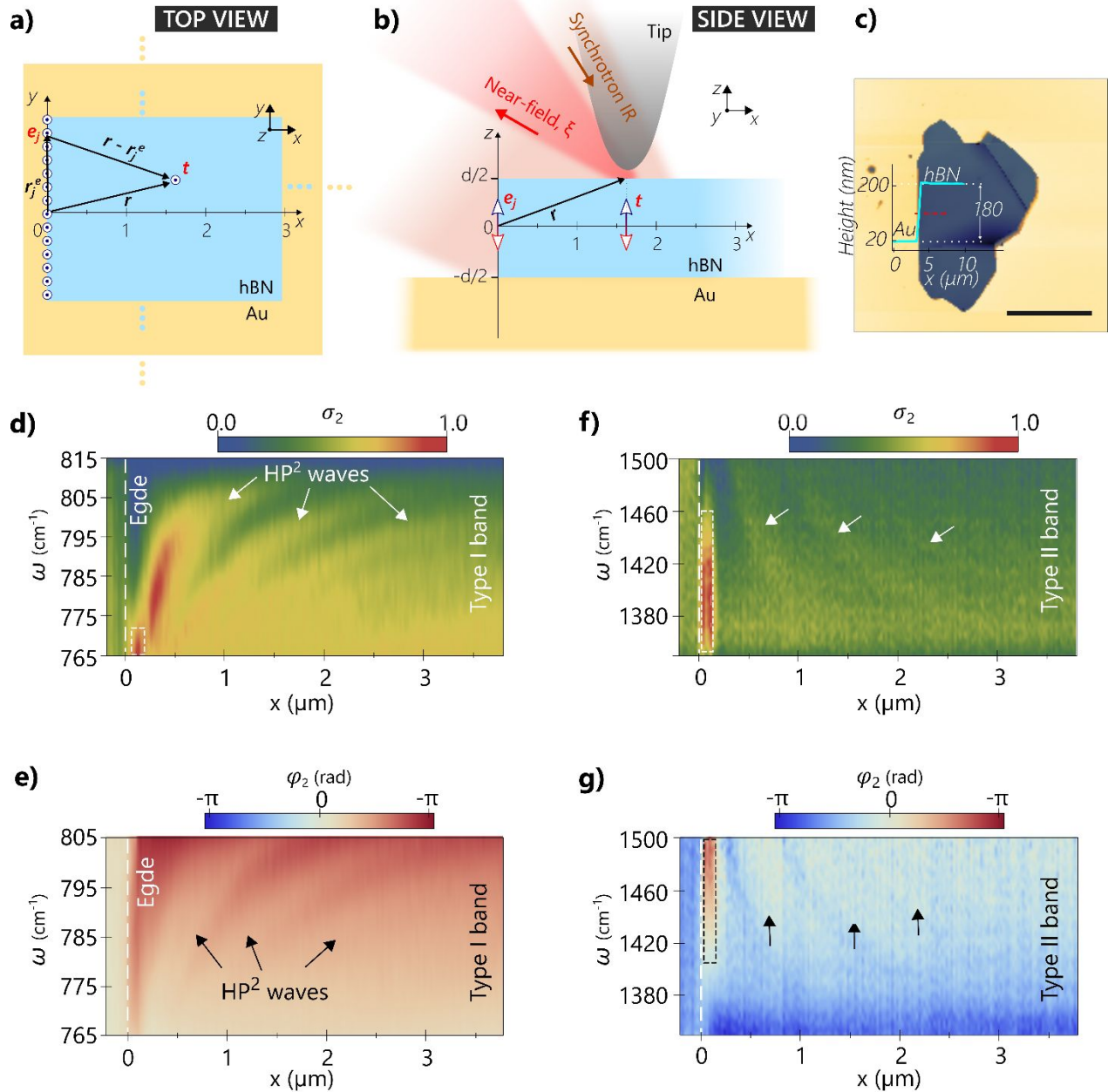


Figure 1 – SINS spectral linescan in the type I and II hyperbolic bands of hBN lying on Au surface. (a) $y - x$ (top view) and (b) $z - x$ (side view) planes of the reference frame adopted for the HDA model featuring the SINS experiment in the hBN/Au. The tip (t) and edge (e) dipoles are positioned at x and $x = 0$, respectively. (c) AFM topography of the 180 nm-thick hBN crystal as seen from the height \times distance (x , in micrometers) profile (scale bar: 10 μm). The red dashed line marks the acquisition location of the spectral linescan in (d-g). (d) Normalized amplitude σ_2 and (e) phase φ_2 spectral linescans over the type I band. (f) σ_2 and (g) φ_2 spectral linescan over the type II band. Arrows in (d-g) highlight contrasting spatio-spectral branches corresponding to HP² waves. The rectangles in (d), (f) and (g) mark the appearance of modes, within 200 nm from the hBN edge, which are distinct from the volume confined HP²s. The spectral linescans were collected with 3.57 cm^{-1} spectral resolution.

Spectral linescans and the HDA model. Figure 1b illustrates the SINS spectral linescan across the edge of a hBN crystal lying on Au surface (Figure 1c) and the reference frame for the HDA model. Figure 1c displays the AFM topography of the 180 nm thick hBN crystal analyzed by SINS in Figure 1 d-g. The amplitude (σ_2) and phase (φ_2) spectral linescans, over the type I and, are shown in Figure 1d and 1e, respectively. The corresponding spectral linescan, over type II band, are presented in Figure 1f and 1g. These measurements reveal modes (rectangles in Figure 1d, 1f and 1g), within 200 nm from the crystal edges. Yet appearing much more close to the crystal edges in this case of Au as substrate, such modes can be analogues to the surface or edge polaritons reported for hBN/SiO₂ systems^{15,30}. They are clearly distinguishable from the volume confined HP²s, with onset for $x \geq 250$ nm, which are the only analyzed in this work.

HP²s rise because the IR illumination induces intense optical near-field concentrations causing strong optical polarizations near the tip and the crystal edge. Those polarized locations gather resonant radiation and enough momenta to excite polaritons in hBN, thus, being turned into sources of the HP² waves. Thereby, the resulting polaritonic field is created from the interference among tip- and edge-launched waves and a non-propagating response. As already reported^{6,8}, tip-launched waves travel towards the crystal edge, where, they get reflected and propagate back to the tip. Edge-launched waves propagate directly towards the tip. As a consequence of the different hyperbolicities of each band, the distance between maxima of the spectral linescan increase with ω in the type I band (Figure 1d and 1e), but the contrary trend happens in the type II band (Figure 1f and 1g). As discussed below, this signifies that q_p s of type I HP²s shorten as ω increases, whilst the opposite behavior is found in the type II band.

For a given excitation ω ($\omega = \text{constant}$), the horizontal profiles extracted from the spectral linescans correspond to a HP² wave as function of the distance x from the crystal edge. The lineshapes of σ_2 and φ_2 for $\omega = 795$ cm⁻¹, taken from the Figure 1d and 1e, respectively, are plotted in Figure 2a and 2b. Analogue profiles for $\omega = 1465$ cm⁻¹, extracted from Figure 1f and 1g, are presented in Figure 2c and 2d. To interpret those polariton waves within the HDA model, we consider the tip dipole (t) at r and N dipoles (e_i) distributed along the edge (Figure 1a). The position of the tip dipole varies with the tip scanning, while each e_i is fixed and positioned at r_j^e . The separation between the individual e_i 's is 30 nm. All dipoles are oriented in the z -axis since the tip geometry privileges launching/detecting of z -polarized fields as confirmed by the numerical simulations shown in Figure 2e (see methods). Those calculations reveal that the z -polarized field of a HP² wave irradiated from a tip-like antenna (Figure 2f) is the dominant component to the total field. With these considerations, the resulting polariton field E_z is given by Equation 1 whose first and second terms are the tip and edge fields, respectively. The third term is the non-propagating tip-sample response, which is characterized by the asymptotic values of the polariton waves in the limit wherein they are completely damped. The electric fields of the tip and edge dipoles are expressed in terms of the amplitudes A and B_j , the propagated distances from their sources, the angles θ_t and θ_j^e , defined between the dipole orientation (z -axis) and the unit vectors \hat{r}_t and \hat{r}_j^e , and the relative phase difference ϕ between the wave emitted by tip and edge dipoles. The complex momentum $k = q_p + i\kappa_p$ is defined by the in-plane momentum q_p (real part) and the damping κ_p (imaginary part), respectively. The non-propagating response has the amplitude C and phase α . See the supporting information for more details on the model. The correspondence between equation 1, written as $E_z = |E_z|e^{i\psi}$,

and the measured near field $\xi_2 = \sigma_2^{-i\varphi_2}$ is accomplished by the identities $|E_z| \equiv \sigma_2$ and $\psi \equiv \varphi_2$. Thereby, we first apply the model to fit the polariton profiles (Figure 2a and 2c) extracted from the spectral linescan (Figure 1d and 1f). The fitting equation 1 considers one edge dipole ($j = 1$) because the spectral linescan is performed on single path over the sample, hence, being a one-dimensional measurement (Figure 1a). In sequence, we use the Equation 1, taking into the account the sum of all edge dipoles, to simulate amplitude maps (Figure 4) obtained from hyperspectral images.

$$E_z(r) = -ikA \frac{e^{-ik(|\vec{r}_t| + \phi)}}{4\pi|\vec{r}_t|} \sin^2 \theta_t - \sum_{j=1}^N ikB_j \frac{e^{-ik|\vec{r} - \vec{r}_j^e|}}{4\pi|\vec{r} - \vec{r}_j^e|} \sin^2 \theta_j^e + Ce^{-i\alpha} \quad (1)$$

$$k(\omega) = -\frac{\Lambda}{d} \left[\arctan\left(\frac{\epsilon_a}{\epsilon_{\perp} \Lambda}\right) + \arctan\left(\frac{\epsilon_s}{\epsilon_{\perp} \Lambda}\right) + \pi l \right] \quad (2)$$

$$\Lambda = -i \sqrt{\frac{\epsilon_{\parallel}}{\epsilon_{\perp}}} \quad (3)$$

The fits of $|E_z|$ (red solid lines) to the experimental σ_2 's (circles), for $\omega = 795 \text{ cm}^{-1}$ and $\omega = 1465 \text{ cm}^{-1}$, are presented in Figure 2a and 2c, respectively. Such fits are done for $z = d/2$, the upper crystal surface. In sequence, the fit-extracted parameters (k , A_E , A_t , ϕ , C and α) are used as inputs to generate the HDA phases ψ 's, which are plotted with the corresponding experimental φ_2 's in Figure 2b and 2d. Such theoretical and experimental phase curves were overlapped only by the adjust of the baseline. It is observed that ψ 's describe very well φ_2 profiles with good match of lineshapes. Furthermore, Figure 2f exhibits the correspondence between the phasor of the complex-valued fit-generated E_z and the measured phasor of ξ_2 . We note that the HDA model, self-consistently, provides an accurate determination of the properties of the HP² waves and the reconstruction of the full complex-valued ξ_2 .

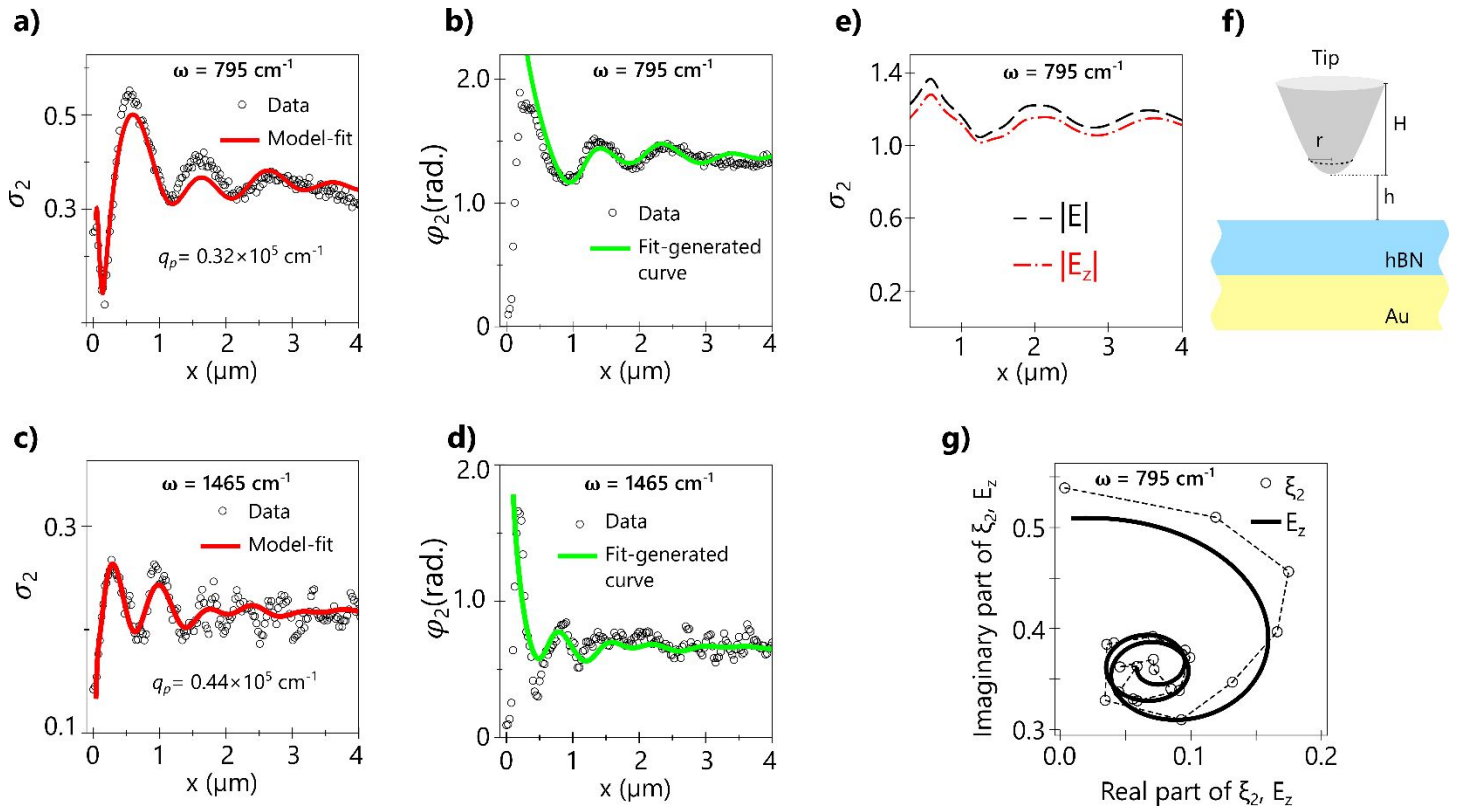


Figure 2 – **HDA model fits to HP² waves.** (a) σ_2 profile for $\omega = 795 \text{ cm}^{-1}$. (\circ), extracted from the type I band spectral linescans in Figure 1d, and the corresponding fit curve (red solid line). (b) φ_2 profile (\circ) and the corresponding fit-generated phase (green solid line) for $\omega = 795 \text{ cm}^{-1}$. The amplitude fit (c) and the experimental and generated phase (d) are presented for $\omega = 1465 \text{ cm}^{-1}$ in type II band. (e) Numerical simulations of the E and E_z fields of tip-launched HP²s in hBN (180 nm thick) on Au considering the illustration (f) where the tip, placed far from any crystal edges, is represented by a conic of rounded apex with $r = 25 \text{ nm}$, $h = 40 \text{ nm}$ and $H = 625 \text{ nm}$ (see methods for details). (g) Phasor of the experimental ξ_2 (symbols \circ connected by the dashed guideline) and the phasor of the fit-generated E_z (black curve) for $\omega = 795 \text{ cm}^{-1}$.

The fits of σ_2 profiles over the type I and II bands allow obtaining their $\omega - q_p$'s in good agreement with the predicted curves from equations 2 and 3 for the fundamental polariton branch⁴ $n = 0$ (Figures 3a and 3b). In those equations, the indexes a, s, \perp and \parallel denote, respectively, air superstrate, Au substrate, in- and out-of-plane components of $\vec{\epsilon}$ of the hBN crystal. These results can be confirmed from several reports on the type II band, for different hBN-based systems, and, recently, on type I band⁶ addressing hBN/Au. Nevertheless, SINS enables investigating a more extended range of the out-of-plane polaritons waves revealing that, albeit both types of HP²s present similar momentum on Au substrate, the confinement factor (λ_{lr}/λ_p) in the type I band surpasses by nearly 3 times that in the type II one: $\lambda_{lr}/\lambda_p \sim 18$, for $\omega = 776 \text{ cm}^{-1}$, in the type I band, whereas, $\lambda_{lr}/\lambda_p \sim 6$, for $\omega = 1479 \text{ cm}^{-1}$ in the type II band. The model yields also comparably good results for a 45 nm- and a 90 nm-thick hBN crystals on Au and SiO₂, respectively (see supporting information). For the 45 nm thick hBN/Au, we observe $\lambda_{lr}/\lambda_p \sim 30$, for $\omega = 790 \text{ cm}^{-1}$, approaching the highest values reported¹.

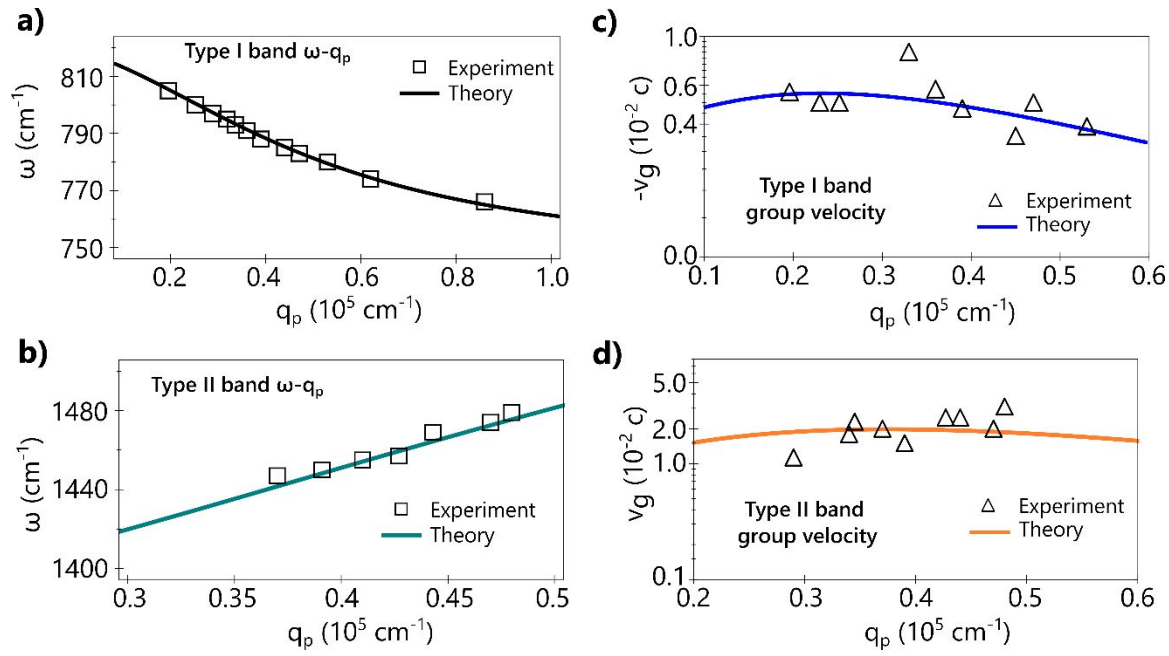


Figure 3 – $\omega - q_p$'s and group velocities v_g 's of the two types of HP²s. (a) Fit-extracted (squares) and (b) theoretical (curves) $\omega - q_p$'s for type I and type II HP²s, respectively. (c) Fit-determined and (d) theoretical v_g 's of the type I and type II HP²s, respectively. The theoretical curves in (a, b) correspond to the fundamental mode ($n = 0$) of the equation 2 for both bands.

Using the definition³⁶ $v_g = 2\pi c \frac{d\omega}{dq_p}$ (c is the velocity of light in vacuum), the v_g 's of the type I (Figure 3c) and type II (Figure 3d) polariton pulses are determined from the corresponding fit-extracted and theoretical $\omega - q_p$'s in Figure 3a and 3b, respectively. In analogy to previous report²³, we find negative v_g for type I HP²s (Figure 3b) and positive v_g for type II polaritons (Figure 3d), both agreeing with theory. Type I pulse at $\omega = 800 \text{ cm}^{-1}$ is nearly 100 times slower than the light in vacuum presenting a lifetime $\tau \sim 0.6 \text{ ps}$ ($\tau = L/|v_g|$, where $L = 1/\kappa_p$ is the propagation length for amplitude decay at $1/e$)²¹. In contrast, type II pulse at $\omega = 1447 \text{ cm}^{-1}$ presents shorter $\tau_g \sim 0.3 \text{ ps}$. Note that $\omega = 800 \text{ cm}^{-1}$ and 1447 cm^{-1} ω occupy central positions in their respective bands, thus, being good representatives of the polaritonic pulses. Such values of τ are similar to those found from time-domain interferometry combined with s-SNOM experiments²¹ indicating that our model also determines reasonable values of κ_p . For the 45 nm-thick hBN on Au, $\tau \sim 1.7 \text{ ps}$ at $\omega = 800 \text{ cm}^{-1}$ (see supporting information) approaches values (2-3 ps) predicted for a suspended hBN crystal, hence, free of substrate induced losses³⁰.

Hyperspectral images: experiment and simulations. Figure 4a and 4b display σ_2 images of type I and type II HP²s obtained from SINS hyperspectral images (see Methods for details) on different hBN flakes on Au. In both measurements, the geometrical pattern of the polariton standing waves is dictated by the form of the crystal edges (indicated by white dashed lines). It is important to stress again that, whilst type II HP² waves have been imaged in several hBN systems by s-SNOM using narrow-band lasers, σ_2 images for type I HP²s, shown here by SINS, were depicted using space-time s-SNOM mapping on hBN/SiO₂²¹ and, recently, by means of PiFM in hBN/Au⁶. In analogy with those reports, we can state that the

SINS hyperspectral images, while recording concomitantly the type I and type II polaritonic fields (see supporting information), possess sensitivity comparable to those obtained with lasers.

To simulate the measured σ_2 images in Figure 4a and 4b, we use the Equation 1 with one HDA at the tip location and regular distributions of HDAs along the crystal edges with one dipole at each 30 nm, as illustrated in Figure 4c and 4d. For edges relatively oriented with the angle $\beta \leq 90^\circ$ (Figure 4b), the tip contributes with more the one term, similarly to the method in ref. 4. The non-propagating field in Equation 1 is given by the point-spectrum, without influence of the polariton oscillations, calculated from the generalized spectral method³⁷. In the simulations, we use the momentum k given by the analytic Equation 2 and 3. But the model can also suit to general expressions³⁸ for $\omega - q_p$ with numerical solutions. The resulting simulations are shown in Figure 4e and 4f in good accordance with the respective experiments in Figure 4a and 4b. The accurate agreement is also verified by the comparison of profiles extracted from experiments (black curves) and simulations (red curves) shown in Figure 4g and 4h. We note that our simulation results are comparable with the recently published multiplebeam interference (MBI) model³⁹. Regardless the fact that the MBI model use different spatial functions and more components to describe the polariton waves, both modellings have a convergent interpretation by considering oscillating terms originated at the edge, at the tip and a non-propagating term.

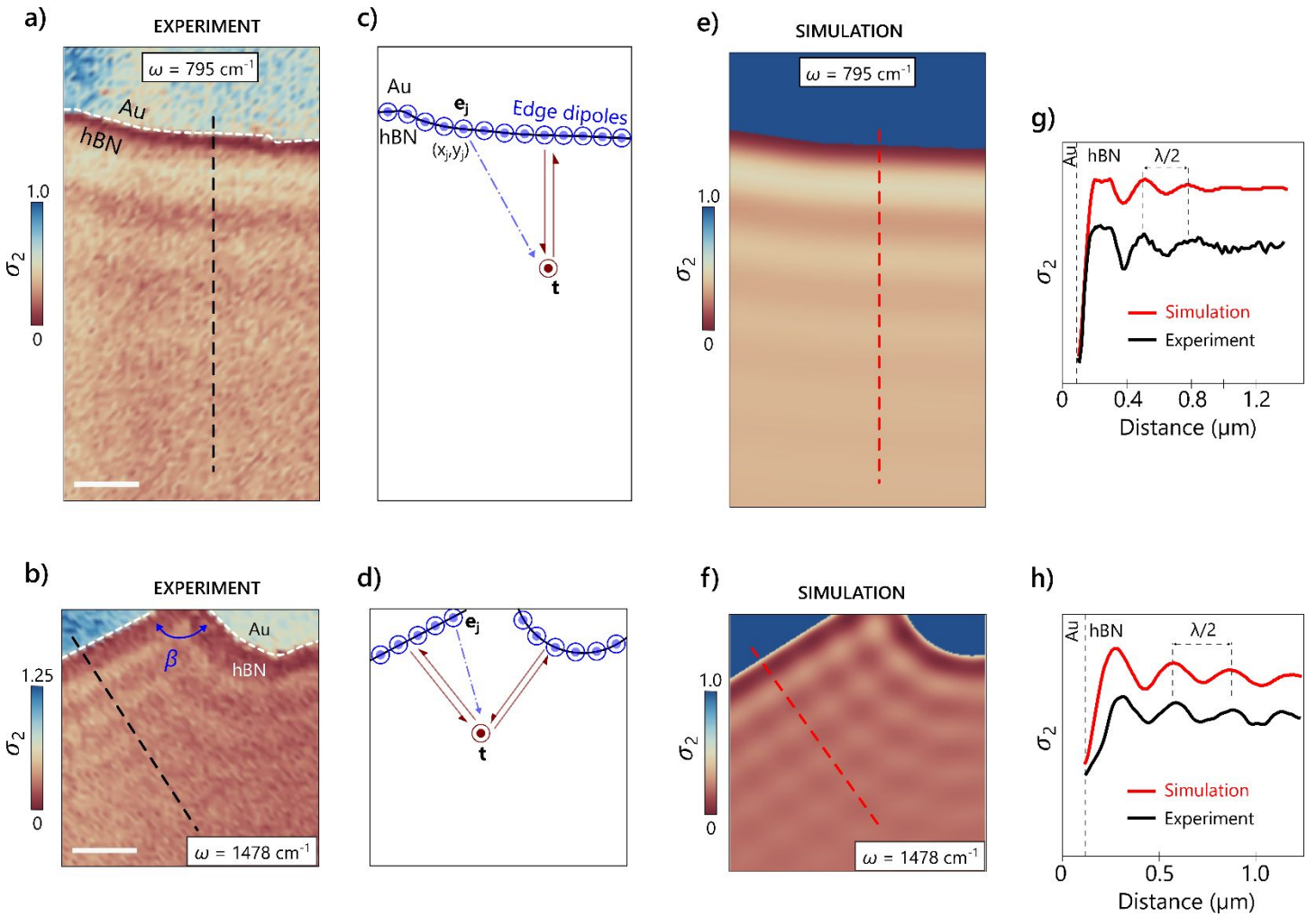


Figure 4 – **Hyperspectral images-generated amplitude maps and respective HDA simulations of HP²waves.** Experimental σ_2 images of (a) $\omega = 795 \text{ cm}^{-1}$ (type I band) and (b) $\omega = 1478 \text{ cm}^{-1}$ (type II band). (c and d) Configuration of the tip and edge dipoles to the simulated images in (e) and (f), respectively. (g and h) profiles extracted from experimental (a and b) and simulated (e and f) images. Measurements (a and b) have been post-processed from hyperspectral images. Image (a) was acquired from 100 nm thick hBN on a $3.5 \mu\text{m} \times 2 \mu\text{m}$ area, segmented in $60 \text{ px} \times 60 \text{ px}$, with spectral resolution of 10 cm^{-1} . Image (b) was acquired from a 90 nm-thick hBN on $2 \mu\text{m} \times 2 \mu\text{m}$ area, segmented in $100 \text{ px} \times 57 \text{ px}$, with spectral resolution of 6.25 cm^{-1} . Scale bar: 500 nm.

Conclusion. In summary, we demonstrate that the HDA model presents good performance for fitting HP²s waves of hBN crystals with different thicknesses on Au and on SiO₂. The fits to polariton amplitude not only lead to accurate convergence between experimental and theoretical $\omega - q_p$'s, but also permit reconstructing the corresponding phase in close agreement with the measurement. Concerning the adopted reference frame (Figure 2e), we find on Au substrate negative group velocity $v_g = -1.5 \times 10^6 \text{ m/s}$, for polaritons in the type I band, and positive $v_g = 6.0 \times 10^6 \text{ m/s}$ for those in the type II band. Those values are similar to the reported for surface HP² modes⁴⁰ and experimental observations²¹ for hBN/SiO₂. It is noteworthy commenting that the v_g signal dictates the direction of the in-plane time-averaged Poynting vector^{3,36} $S_x = v_g \langle u \rangle$, where u is the scalar time-averaged positive energy density. Hence, we observe $S_x > 0$, for type II HP²s, yet, $S_x < 0$ for type I HP²s. Accordingly, the energy flux, associated to S_x , for the type I polaritonic pulse is also anti-parallel to that of the

type II pulse. On Au, the low value of group velocity and small damping produce $\tau \sim 0.6$ ps, for type I HP²s, and ~ 0.3 ps, for type II HP²s, which are longer than those found on SiO₂^{21,30} and comparable to the timescale of plasmons polaritons⁴⁰, hybrid plasmons phonons polaritons⁴¹ and excitons polaritons active in polaritonic lasers⁴². Furthermore, the correspondence between simulated and measured amplitude images, for the two polariton types in crystals of distinct geometries, confirms that the total electric field emitted from dipole sources can reliably be used to represent the polariton waves. Our model is not restricted to HP²s, hence, being applicable to other types of polaritons, like plasmon-polaritons in graphene³⁵ and exciton-polaritons in vdW transition metal dichalcogenides^{43,44}.

Methods

Synchrotron infrared nanospectroscopy (SINS). SINS is performed at the infrared nano-spectroscopy beamline of the Brazilian Synchrotron Light Laboratory (LNLS)²⁷. In SINS, broadband synchrotron mid-IR radiation is the excitation source for a commercial s-SNOM microscope (neaSNOM by NeaSpec GmbH). This nanoscope, summarily, consists of an atomic force microscope (AFM) equipped with the suited optics to probe the optical near-field. For SINS, the AFM is set in semi-contact mode, wherein, a metal-coated AFM tip (ARROW-NCpt-W, NANO WORLD) is, electronically, driven to vibrate in its natural mechanical frequency Ω that modulates the tip-sample height $h(t) \propto A \cdot \cos(\Omega t)$, where A is the oscillating amplitude. Here, we set $A \sim 80$ nm for the tip with $W \sim 300$ kHz. In this semi-contact mode, the IR beam is focused on the tip-sample system causing charge separation of the metal-coating of the tip, inducing the antenna phenomenon to the tip. This nanoantenna, thus, acts converting incident (far-field) radiation in highly intense optical near-field that, in its turn, induces a local effective polarization to the medium. The nanoantenna (tip) scatters back to the detector the complex optical near-field ξ (Figure 1a) originated from the effective polarization location, i.e., from the spatial volume between the tip apex and $h(t)$. The sub-diffractive optical resolution of SINS (and s-SNOM) stems from fact that ξ comes from a region defined by the radius r of the tip apex ($r \sim 25$ nm, in our case) that which much smaller than the limit of diffraction of the mid-IR excitation wavelengths ranging from 3 to 15 μ m in our setup. In the detection scheme, the light coming from the tip-sample system reaches a Mercury Cadmium Telluride detector (MCT, IR-Associates). This scattered light carries ξ and a strong component of far-field radiation. Legitimate ξ , free from far-field contribution, is given by the light modulated at the high harmonics n of W , for $n \geq 2$. The demodulation of the high harmonic components of ξ is made by a lock-in based-electronics. Here, we present data with respect to $n = 2$, the optical second harmonic ξ_2 . Like s-SNOM, SINS is sensitive to the amplitude and phase of ξ_2 . The spectroscopy is accomplished by interferometry between ξ_2 and a far-field reference arm using an asymmetric Michelson interferometer. The Fourier Transform of the corresponding interferogram yields the amplitude $\sigma_2(\omega)$ and -phase $\varphi_2(\omega)$ spectra²⁷, where $\xi_2 = \sigma'_2(\omega) e^{-i\varphi_2(\omega)}$. Normalized spectra with respect to Au near-field response ($\xi_{2,Au} = \sigma'_{2,Au} e^{-i\varphi'_{2,Au}}$) are referred here as to $\sigma_2(\omega) = \frac{\sigma'_2(\omega)}{\sigma'_{2,Au}(\omega)}$, for the amplitude, and $\varphi_2(\omega) = \varphi'_2(\omega) - \varphi_{2,Au}(\omega)$, for the phase. In this work, we have performed spectral linescans, where a set of sequential point-spectra are acquired on a pre-defined path (1D) rendering spatio-spectral maps (Figures 1d-f) and hyperspectral images, a set of point-spectra are recorded at each pixel over a $W \times L$ area segmented in $N \times M$ pixels. Post-processing the hyperspectral images data produces 2D single- ω maps (Figure 4a and 4b).

Sample Preparation. The construction of the sample substrate consisted of the deposition of a 5 nm thick layer of Cr on the surface of a highly doped Si wafer ($10 \times 10 \times 1$ mm³). In sequence, a 100 nm thick film of Au was grown on the Cr surface (5 nm Cr layer was used to strengthen the Au adhesion). Both Au and Cr films depositions were done by sputtering. The hBN crystals, purchased from HQ Graphene, were deposited atop Au surface by mechanical exfoliation (Scotch tape method).

Numerical Simulations. Finite-Difference Time-Domain (FDTD) simulations (Lumerical Inc. v8.21) was used to calculate the tip-launched HP²s profiles presented in Figure 2e. The AFM tip was modeled as a rounded tip cone made of

Platinum with tip radius, height, cone angle of 25nm, 670nm and 25 °, respectively. The distance of the tip to the surface was 40 nm. Optical properties of Au and Pt were obtained from Palik (Handbook of Optical Constants of Solids I - III by E. Palik). Additionally, the complex dielectric function of the 180nm-thick hBN crystal was calculated from Lorentz-Drude model. The simulation time was 10 ps and the simulation region was bounded with perfectly matched layer (PML) absorbing boundaries. At region of the apex of the tip, the mesh size was reduced to 8 nm in the X and Y directions and 5 nm in the Z direction. Notwithstanding, a gaussian source with thin lens approximation and incident angle of 30 ° illuminated the tip from above. A line frequency monitor located at 80 nm above the hBN crystal measured the electromagnetic field components. Furthermore, this simulation was also performed on a semi-infinite solid made of gold separated by 40 nm from the Pt tip apex. The electric field components collected from the simulation on hBN was normalized by the magnitude of the electric field from simulation on gold, thereby giving the results in amplitude units as in experiment.

Acknowledgements. All authors thank the Brazilian Synchrotron Light Laboratory (LNLS) for providing beamtime for the experiments. We are grateful to Yves Petroff for the fruitful discussions and for revising the work. NeaSpec GmbH is thanked for the technical support. Angelo L. Gobbi and Maria H. de Oliveira Piazzetta, from the Brazilian Nanotechnology National Laboratory, are acknowledged for the assistance in sample construction. F.C.B.M. and F.H.F acknowledge the FAPESP project 2018/05425-3. R.O.F. and R.M. acknowledge the FAPESP project 2019/08818-9. R.O.F. acknowledge CNPq for the research grant 311564/2018-6. D.A.B. acknowledges support from FAPESP projects 2015/11779-4 and 2018/07276-5, the Brazilian Nanocarbon Institute of Science and Technology (INCT/Nanocarbono), the National Council for Scientific and Technological Development – CNPq and MackPesquisa. This work was partially supported by the Brazilian Institute of Science and Technology (INCT) in Carbon Nanomaterials and the Brazilian agencies CAPES and CNPq. M.B.R. acknowledges support from the U. S. Department of Energy, Office of Basic Sciences, Division of Material Sciences and Engineering, under award no. DE-SC0008807.

References

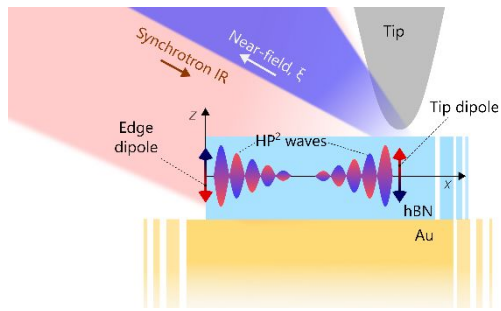
- 1 D. N. Basov, M. M. Fogler and F. J. Garcia de Abajo, *Science (80-)*, 2016, **354**, aag1992 1-8.
- 2 T. Low, A. Chaves, J. D. Caldwell, A. Kumar, N. X. Fang, P. Avouris, T. F. Heinz, F. Guinea, L. Martin-Moreno and F. Koppens, *Nat Mater*, 2017, **16**, 182–194.
- 3 D. L. Mills, E. Burstein and V. Gunawan, *Reports Prog Phys*, 1974, **37**, 817–926.
- 4 S. Dai, Z. Fei, Q. Ma, A. S. Rodin, M. Wagner, A. S. McLeod, M. K. Liu, W. Gannett, W. Regan, K. Watanabe, T. Taniguchi, M. Thiemens, G. Dominguez, A. H. Castro Neto, A. Zettl, F. Keilmann, P. Jarillo-Herrero, M. M. Fogler and D. N. Basov, *Science (80-)*, 2014, **343**, 1125–1129.
- 5 A. Poddubny, I. Iorsh, P. Belov and Y. Kivshar, *Nat Photonics*, 2013, **7**, 948–957.

- 6 A. Ambrosio, M. Tamagnone, K. Chaudhary, L. A. Jauregui, P. Kim, W. L. Wilson and F. Capasso, *Light Sci Appl*, 2018, **7**, 27.
- 7 L. V. Brown, M. Davanco, Z. Sun, A. Kretinin, Y. Chen, J. R. Matson, I. Vurgaftman, N. Sharac, A. J. Giles, M. M. Fogler, T. Taniguchi, K. Watanabe, K. S. Novoselov, S. A. Maier, A. Centrone and J. D. Caldwell, *Nano Lett*, 2018, **18**, 1628–1636.
- 8 M. Tamagnone, A. Ambrosio, K. Chaudhary, L. A. Jauregui, P. Kim, W. L. Wilson and F. Capasso, *Sci Adv*, 2018, **4**, 4–10.
- 9 Z. Fei, G. O. Andreev, W. Bao, L. M. Zhang, A. S. McLeod, C. Wang, M. K. Stewart, Z. Zhao, G. Dominguez, M. Thiemens, M. M. Fogler, M. J. Tauber, A. H. Castro-Neto, C. N. Lau, F. Keilmann and D. N. Basov, *Nano Lett*, 2011, **11**, 4701–4705.
- 10 F. Keilmann and R. Hillenbrand, *Philos Trans A Math Phys Eng Sci*, 2004, **362**, 787–805.
- 11 X. Chen, D. Hu, R. Mescall, G. You, D. N. Basov, Q. Dai and M. Liu, *Adv Mater*, 2019, **31**, 1–24.
- 12 I. D. Barcelos, A. R. Cadore, L. C. Campos, A. Malachias, K. Watanabe, T. Taniguchi, F. C. B. Maia, R. Freitas and C. Deneke, *Nanoscale*, 2015, **7**, 11620–11625.
- 13 Z. Shi, H. A. Bechtel, S. Berweger, Y. Sun, B. Zeng, C. Jin, H. Chang, M. C. Martin, M. B. Raschke and F. Wang, *ACS Photonics*, 2015, **2**, 790–796.
- 14 T. U. Tumkur, X. Yang, B. Cerjan, N. J. Halas, P. Nordlander and I. Thomann, *Nano Lett*, 2016, **16**, 7942–7949.
- 15 S. Dai, M. Tymchenko, Y. Yang, Q. Ma, M. Pita-Vidal, K. Watanabe, T. Taniguchi, P. Jarillo-Herrero, M. M. Fogler, A. Alù and D. N. Basov, *Adv Mater*, 2018, **30**, 1–5.
- 16 J. Duan, R. Chen, J. Li, K. Jin, Z. Sun and J. Chen, *Adv Mater*, 2017, **1702494**, 1702494.
- 17 S. Dai, Q. Ma, Y. Yang, J. Rosenfeld, M. D. Goldflam, A. McLeod, Z. Sun, T. I. Andersen, Z. Fei, M. Liu, Y. Shao, K. Watanabe, T. Taniguchi, M. Thiemens, F. Keilmann, P. Jarillo-Herrero, M. M. Fogler and D. N. Basov, *Nano Lett*, 2017, **17**, 5285–5290.
- 18 F. C. B. Maia, B. O’Callahan, A. R. Cadore, I. D. Barcelos, L. C. Campos, K. Watanabe, T. Taniguchi, C. Deneke, A. Belyanin, M. B. Raschke and R. O. Freitas, *Nano Lett*, 2019, [acs.nanolett.8b03732](https://doi.org/10.1021/acs.nanolett.8b03732).
- 19 C. Ciano, V. Giliberti, M. Ortolani and L. Baldassarre, *Appl Phys Lett*, 2018, **112**, 153101.
- 20 J. Duan, R. Chen, J. Li, K. Jin, Z. Sun and J. Chen, *Adv Mater*, 2017, **29**, 1702494.

- 21 E. Yoxall, M. Schnell, A. Y. Nikitin, O. Txoperena, A. Woessner, M. B. Lundeberg, F. Casanova, L. E. Hueso, F. H. L. Koppens and R. Hillenbrand, *Nat Photonics*, 2015, **9**, 674–679.
- 22 P. Li, M. Lewin, A. V. Kretinin, J. D. Caldwell, K. S. Novoselov, T. Taniguchi, K. Watanabe, F. Gaussmann and T. Taubner, *Nat Commun*, 2015, **6**, 7507.
- 23 S. Dai, Q. Ma, T. Andersen, a. S. Mcleod, Z. Fei, M. K. Liu, M. Wagner, K. Watanabe, T. Taniguchi, M. Thiemens, F. Keilmann, P. Jarillo-Herrero, M. M. Fogler and D. N. Basov, *Nat Commun*, 2015, **6**, 6963.
- 24 F. J. Alfaro-Mozaz, P. Alonso-González, S. Vélez, I. Dolado, M. Autore, S. Mastel, F. Casanova, L. E. Hueso, P. Li, A. Y. Nikitin, R. Hillenbrand and & R. Hillenbrand, *Nat Commun*, 2017, **8**, 15624.
- 25 P. Li, I. Dolado, F. J. Alfaro-Mozaz, F. Casanova, L. E. Hueso, S. Liu, J. H. Edgar, A. Y. Nikitin, S. Vélez and R. Hillenbrand, *Science (80-)*, 2018, **359**, 892–896.
- 26 S. Dai, Q. Ma, M. K. Liu, T. Andersen, Z. Fei, M. D. Goldflam, M. Wagner, K. Watanabe, T. Taniguchi, M. Thiemens, F. Keilmann, G. C. a. M. Janssen, S.-E. Zhu, P. Jarillo-Herrero, M. M. Fogler and D. N. Basov, *Nat Nanotechnol*, 2015, **10**, 682–686.
- 27 R. O. Freitas, C. Deneke, F. C. B. Maia, H. G. Medeiros, T. Moreno, P. Dumas, Y. Petroff and H. Westfahl, *Opt Express*, 2018, **26**, 11238.
- 28 H. A. Bechtel, E. A. Muller, R. L. Olmon, M. C. Martin and M. B. Raschke, *Proc Natl Acad Sci U S A*, 2014, **111**, 7191–6.
- 29 B. Pollard, F. C. B. Maia, M. B. Raschke and R. O. Freitas, *Nano Lett*, 2016, **16**, 55–61.
- 30 P. Li, I. Dolado, F. J. Alfaro-Mozaz, A. Y. Nikitin, F. Casanova, L. E. Hueso, S. Vélez and R. Hillenbrand, *Nano Lett*, 2017, **17**, 228–235.
- 31 F. C. B. Maia, B. T. O’Callahan, A. R. Cadore, I. D. Barcelos, L. C. Campos, K. Watanabe, T. Taniguchi, C. Deneke, A. Belyanin, M. B. Raschke and R. O. Freitas, *Nano Lett*, 2019, **19**, 708–715.
- 32 W. Ma, P. Alonso-González, S. Li, A. Y. Nikitin, J. Yuan, J. Martín-Sánchez, J. Taboada-Gutiérrez, I. Amenabar, P. Li, S. Vélez, C. Tollan, Z. Dai, Y. Zhang, S. Sriram, K. Kalantar-Zadeh, S. T. Lee, R. Hillenbrand and Q. Bao, *Nature*, 2018, **562**, 557–562.
- 33 L. Gilburd, K. S. Kim, K. Ho, D. Trajanoski, A. Maiti, D. Halverson, S. De Beer and G. C. Walker, *J Phys Chem Lett*, 2017, **8**, 2158–2162.
- 34 M. Tamagnone, A. Ambrosio, K. Chaudhary, L. A. Jauregui, P. Kim, W. L. Wilson and F. Capasso, *Sci Adv*, 2018, **4**, eaat7189.

- 35 A. Woessner, M. B. Lundeberg, Y. Gao, A. Principi, P. Alonso-González, M. Carrega, K. Watanabe, T. Taniguchi, G. Vignale, M. Polini, J. Hone, R. Hillenbrand and F. H. L. Koppens, *Nat Mater*, 2014, **14**, 421–425.
- 36 J. D. Jackson, *Classical Electrodynamics*, Wiley, Third Edit.
- 37 B. Y. Jiang, L. M. Zhang, A. H. Castro Neto, D. N. Basov and M. M. Fogler, *J Appl Phys*, , DOI:10.1063/1.4941343.
- 38 D. Hu, X. Yang, C. Li, R. Liu, Z. Yao, H. Hu, S. N. G. Corder, J. Chen, Z. Sun, M. Liu and Q. Dai, *Nat Commun*, 2017, **8**, 1471.
- 39 B. Liao, X. Guo, D. Hu, F. Zhai, H. Hu, K. Chen, C. Luo, M. Liu, X. Yang and Q. Dai, *Adv Funct Mater*, 2019, **1904662**, 1904662.
- 40 G. X. Ni, A. S. McLeod, Z. Sun, L. Wang, L. Xiong, K. W. Post, S. S. Sunku, B. Y. Jiang, J. Hone, C. R. Dean, M. M. Fogler and D. N. Basov, *Nature*, 2018, **557**, 530–533.
- 41 I. D. Barcelos, A. R. Cadore, A. B. Alencar, F. C. B. Maia, E. Mania, R. F. Oliveira, C. C. B. Bufon, Â. Malachias, R. O. Freitas, R. L. Moreira and H. Chacham, *ACS Photonics*, 2018, **5**, 1912–1918.
- 42 D. Sanvitto and S. Kéna-Cohen, *Nat Mater*, 2016, **15**, 1061–1073.
- 43 M. Mrejen, L. Yadgarov, A. Levanon and H. Suchowski, *Sci Adv*, 2019, **5**, 1–6.
- 44 F. Hu, Y. Luan, M. E. Scott, J. Yan, D. G. Mandrus, X. Xu and Z. Fei, *Nat Photonics*, 2017, **11**, 356–360.

Table of contents entry



Sentence of text highlighting the novelty of the work

Full electromagnetic dipole model for extraction of photonic properties and simulation of polariton waves.